

Impact and lifecycle of superfluid helium drops on a solid surface

Matthew L. Wallace ¹, David Mallin,¹ Michael Milgic ¹, Andres A. Aguirre-Pablo ²,
Kenneth R. Langley ², Sigurdur T. Thoroddsen ² and Peter Taborek¹

¹*Department of Physics and Astronomy, University of California Irvine, Irvine, California 92697, USA*

²*Division of Physical Sciences and Engineering, King Abdullah University of Science and Technology (KAUST), Thuwal 23955-6900, Saudi Arabia*



(Received 27 April 2020; accepted 24 July 2020; published 10 September 2020)

We have used high-speed video and interferometry to investigate the impact, spreading, and eventual contraction of superfluid ^4He drops on a sapphire substrate in a saturated atmosphere of helium vapor. We find that the short-term kinetic spreading of superfluid drops (time $t < 10$ ms) is qualitatively similar to both normal helium and conventional fluids at room temperature. In contrast, the contraction phase of the superfluid drops is highly unusual. Superfluid drops survive for only a few seconds on the substrate due to superflow out of the drop into the surrounding helium film. The drop lifetime is strongly dependent on temperature and diverges at the superfluid transition temperature $T_\lambda \sim 2.17$ K. The contracting drops undergo a geometry-dependent two-phase contraction, which includes a toroidal phase where the radius decreases linearly in time and subsequently a spherical cap phase where the radius decreases with the square root of time. The receding contact angle is temperature dependent and becomes small near T_λ . We also observe that the superfluid outflow causes surprising edge effects, including the emergence of satellite droplets on the perimeter of the expanding drop, as well as ragged and frayed drop edges at lower temperatures.

DOI: [10.1103/PhysRevFluids.5.093602](https://doi.org/10.1103/PhysRevFluids.5.093602)

I. INTRODUCTION

Liquid drop impact and spreading are ubiquitous phenomena with diverse applications. They have been investigated using classical fluids under a wide variety of conditions, including drop impact on a solid dry surface [1–6], on a thin liquid film [7–9], in a deep liquid pool [10], in an atmosphere of ordinary air, and in an atmosphere of air mixed with the fluid’s own vapor [11]. Most of these studies have focused on either short-term (inertia-driven) spreading, driven by the kinetic energy of impact; or on long-term spreading, driven by either surface tension or gravity. The experiments typically record the height H (or thickness) of the impacting/spreading drop and the radius of the drop footprint r as it spreads as a function of time t . For the short-time regime of kinetic impact, the drop radius as a function of time scales as $r(t) \sim t^a$, with $a = 1/2$ for nearly all fluids regardless of wettability due to the balance between interfacial tension and inertia [12,13]. For nonvolatile fluids that completely wet a substrate, a spreading drop will eventually evolve into a pancake shape with a large radius and a microscopic thickness [14]. The approach to this state can be described by power laws $r(t) \sim t^\alpha$, with the exponent α being determined by a balance between the driving forces and dissipation in the drop. For surface-tension-driven spreading of spherical cap drops, $\alpha = 1/10$, which is known as Tanner’s law. Other geometries and driving forces yield values of α in the range 0.1–0.15 [3,15,16]. In the hydrodynamic lubrication approximation limit, the prefactor for the power law is inversely proportional to the fluid’s dynamic viscosity η ; for the

case of gravity-driven spreading [15], the drop radius is given by

$$r(t) \sim V^{3/8} \left(\frac{\rho g t}{\eta} \right)^{1/8}, \quad (1)$$

where ρ is the fluid density, V is the drop volume, and g is the acceleration due to gravity.

Equation (1) shows that, in a classical fluid, the dynamics of spreading are related to viscous dissipation. Superfluids can flow without any dissipation, and even if there is dissipation, the mechanism involves nucleation and generation of vorticity [17], which is quite different from conventional viscous dissipation. For these reasons, theorists have suggested [14,18] that superfluid spreading kinetics might be distinctly different from the classical case. Another assumption that underlies asymptotic predictions such as Eq. (1) is that the fluid completely wets the substrate and that the equilibrium contact angle is zero. Liquid ^4He in both the normal and the superfluid states is thought to completely wet all substrates except cesium [19–22]. There nevertheless are intriguing experimental results which show a finite contact angle in the superfluid state [23–25] on conventional substrates. These observations of a static superfluid meniscus with a finite contact angle are presumably due to thermal inhomogeneities or pinned vorticity.

Our experiment monitors the dynamic contact line of a superfluid drop impinging with an initial velocity of approximately 0.4 m/s onto a sapphire substrate covered by an equilibrium thin adsorbed film of superfluid (de Gennes’ “moist” case [14]). Despite the extremely low viscosity, the initial inertia-driven phase of spreading of the superfluid is remarkably similar to the case of classical fluids, and the kinetic energy of impact is essentially dissipated within 20 ms, resulting in a pancake-shaped drop with a footprint radius roughly 5 times the radius of the initial drop. Rather than continuing to spread like a classical fluid, the superfluid drop contracts with a finite receding contact angle and disappears within a few seconds. The dynamics are qualitatively consistent with a model developed by Herminghaus [25,26] which balances the Bernoulli pressure of a superflow at the critical velocity from the drop into the surrounding film against the Laplace pressure due to the curvature of the drop and the pressure due to van der Waals forces. Although we were initially interested in the dynamics of zero-viscosity spreading, it soon became apparent that superfluid effects were more important for the dynamics.

II. EXPERIMENTAL SETUP

The experimental cell shown in Fig. 1 was contained inside an optical cryostat consisting of a vacuum vessel and two concentric gold-plated copper heat shields held at a temperature of 40 and 4 K, respectively, using a closed-cycle refrigerator, also used in a recent related study on jet breakup [27]. The windows in the shields which provided optical access were constructed using a sandwich structure of KG1 glass (to absorb IR radiation) and sapphire (to provide a thermal link to the shield). The cell itself was equipped with a separately pumped ^4He pot which could maintain the temperature between 1.2 and 5.2 K. The helium drops were formed by applying a small overpressure of 2–50 Torr above the saturated vapor pressure to a flow impedance nozzle made from a glass capillary with an inner diameter of 10 μm and an outer diameter of 365 μm . By adjusting the overpressure, drops with a radius of 0.5 mm would fall from the dropper at predictable intervals of approximately 30 s.

The drops fell ~ 1 cm and impacted onto a cylindrical piece of sapphire 31.7 mm in diameter and 19 mm thick. A small ohmic heater with superconducting leads was glued onto the side of the sapphire to provide heat for clearing the surface of extant liquid helium; the system was allowed to return to equilibrium before measurements were taken. An LED light of wavelength 632 nm was used to illuminate the impact surface. The illumination system and the high-speed camera used for imaging from the side were mounted at a downward angle of 6.4°. A fill line, separate from the dropper line, was used to add or remove helium from the cell; during operation, there was always a reservoir of bulk liquid at the bottom of the cell. For the bottom-view imaging, an aluminum mirror

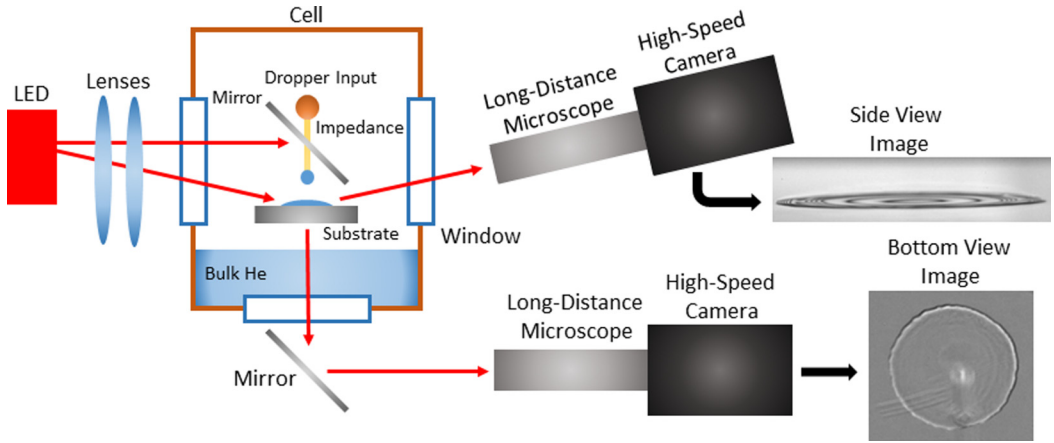


FIG. 1. Schematic diagram of the experimental cell and imaging setup. The cell was mounted inside a cryostat capable of reaching and maintaining temperatures of 1.2–5.2 K. The gravity-fed dropper released the drops onto the sapphire impact surface. A light-emitting diode (LED) and collimating lenses were used to illuminate the drops and the impact surface. Two camera positions were used, one for side viewing and one for bottom viewing. A mirror was used for the bottom viewing, and a hole was drilled in the center of the top mirror, allowing the nanopipe dropper nozzle to pass through.

was used to reflect the light, and an angled hole was drilled in the center of the mirror to allow the capillary nozzle to pass through.

To collect data, the dropper line was pressurized as described above, and the high-speed camera was used to take video of the impacting drops at 100–25,000 frames per second. The individual frames were then extracted from the video and the drop radii measured. In a saturated helium vapor environment, even a nominally “dry” surface is covered with a microscopically thin layer of helium which is stabilized by van der Waals forces. A quartz crystal microbalance (QCM) was occasionally used in place of the sapphire substrate to measure the thickness of this film, but was not used for drop impact and lifecycle measurements. The QCM showed that the equilibrium helium film thickness, presumably limited by the gravitational potential difference between the substrate and the bulk liquid reservoir at the bottom of the cell, was in the range of 20–40 nm thick. The drops were highly mobile on this adsorbed film, and it was important to precisely level the cryostat to prevent the drops from drifting off the edge of the substrate.

Side view images of drops show dark and light fringes due to interference between the liquid-vapor interface at the top of the drop and the liquid-sapphire interface at the bottom of the drop. The change in liquid film thickness per fringe δh (light to light or dark to dark) is

$$\delta h = \frac{\lambda}{2\sqrt{n_{\text{film}}^2 - \sin^2 \theta_{\text{inc}}}}, \quad (2)$$

with light wavelength λ , helium film index of refraction $n_{\text{film}} = 1.03$, and incident angle θ_{inc} . Interference lines were only visible in the side view; in the bottom view, the low index of refraction of liquid helium and the near-normal incidence dictates that the reflected waves from the top drop surface are very weak and are not visible to the camera. These interference lines can be used to determine the drop topography and dynamic contact angle, as discussed in the next section. For images taken with a red LED light with a wavelength of 632 nm and illuminated at an angle $\theta_{\text{inc}} = 83.6^\circ$, each bright fringe corresponds to a change in film thickness of 1167 nm.

III. RESULTS AND DISCUSSION

A. Short-term (inertia-driven) spreading

The physics of inviscid drop impact is governed by a balance between inertia and surface tension and is characterized by the Weber number $We = \rho R U^2 / \gamma$, where R is the drop radius, U is the impact velocity, and γ is the liquid-vapor surface tension. The Weber number in our experiments is ~ 33 for drops impacting at $U = 0.45$ m/s and ~ 145 for drops impacting at $U = 0.94$ m/s. (The experimental results of the drops impacting at $U = 0.94$ are shown only in Fig. 5; all other data presented in this paper is for drops impacting at 0.45 m/s.) During the first few microseconds after impact, the drop shape can be approximated as a truncated sphere, and the spreading radius of the contact line follows the power law $r(t) \sim t^{1/2}$ for geometric reasons [2,7]. The subsequent spreading dynamics can be modeled as a shock [5] or using self-similarity [28,29] at high We or as a singular flow similar to drop coalescence [30,31] for low We . All of these models predict a power-law dependence of the drop footprint radius as a function of time after impact, with an exponent near 1/2; fluid properties affect the prefactor of the power law, but not the exponent. In particular, the inviscid coalescence model predicts

$$r = c \left(\frac{4\gamma A}{\rho} \right)^{1/4} \Delta t^{1/2}, \quad (3)$$

for constant c of order unity (determined to be 2–4 in our experiments), initial radius A , and time $\Delta t = t - t_0$ for time t and initial contact time t_0 . The inertia-driven spreading of fluids with dynamic viscosities in the range of 10^{-3} – 10^0 Pa/s obey a similar power law with the prefactor c determined by the dynamic viscosity [2,13,31]. The inertia-driven shock model of Ref. [5] also predicts a weak dependence of the prefactor on fluid viscosity. In classical fluids, the inertia-driven regime describes the dynamics until the drop footprint has reached approximately three times the original drop diameter, after which the spreading rate slows down and is described by a power law of the form of Eq. (3). A time Δt_{cross} which characterizes the crossover from the inertia-driven regime to capillary-viscous spreading regime is [30]

$$\Delta t_{\text{cross}} = \frac{R^{13/8} \rho^{5/8}}{\eta^{1/4} \gamma^{3/8}}. \quad (4)$$

The crossover time has a typical magnitude of a few milliseconds for our impact velocity and temperature range.

The inertia-driven regime in superfluid impact was monitored using high-speed video from both the side view and the bottom view. A few frames of a side-view video are shown in Fig. 2. Despite the low refractive index, the advancing contact line is clearly visible. A plot of the drop footprint diameter as a function of time for ${}^4\text{He}$ is shown in Fig. 3 for temperatures which span the range from above T_λ to $T = 1.386$ K, where the superfluid fraction is 0.93. After ~ 10 ms, the drops transition to a different regime where the contact line essentially stops moving. Using values for normal ${}^4\text{He}$, Eq. (4) gives a value of 3 ms for the crossover time which is in qualitative agreement with the data. The initial kinetic energy of the drop (approximately 5 nJ) is dissipated within a few milliseconds. In conventional fluids, the dissipation is attributed to complex processes at the moving contact line which are proportional to the viscosity. It is remarkable that a wide variation of the superfluid fraction does not seem to affect the maximum size or the rate of expansion of the drops.

Another interesting feature of the spreading drops is an instability in the advancing contact line that is associated with superfluidity. In contrast to normal ${}^4\text{He}$ fluid drops, which display smooth edge behavior similar to conventional fluids in air at room temperature, superfluid droplets exhibit spatial structure at the edges that becomes increasingly pronounced at lower temperatures and higher superfluid fractions. In our experiment we used two drop impact velocities corresponding to two drop heights. At the lower impact velocity $U = 0.45$ m/s, the superfluid droplets formed rings of

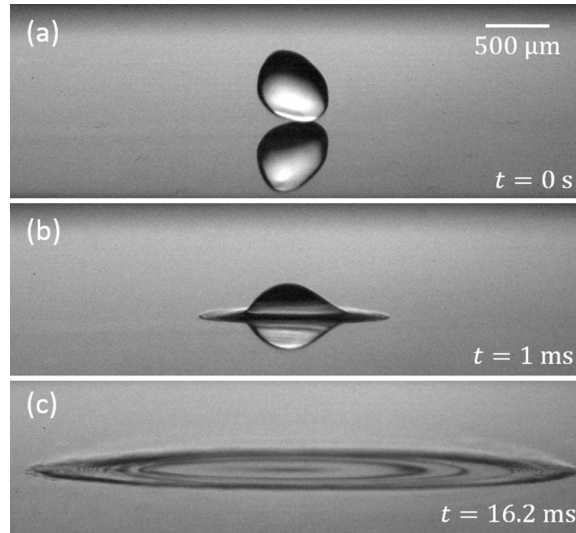


FIG. 2. Short-term spreading of a drop at temperature $T = 1.518$ K impacting on the sapphire substrate shown at time t after impact. Panel (a) shows the drop at the moment of impact, and panel (c) shows the drop near the maximum spreading radius R_{\max} . The concentric bands of light and dark are due to interference from regions of different thicknesses. The image of the drop is reflected in the sapphire surface in panels (a) and (b). Because of the very low viscous dissipation, initial shape perturbations are not damped out in superfluid drops, so they are often remarkably asymmetric, as in panel (a).

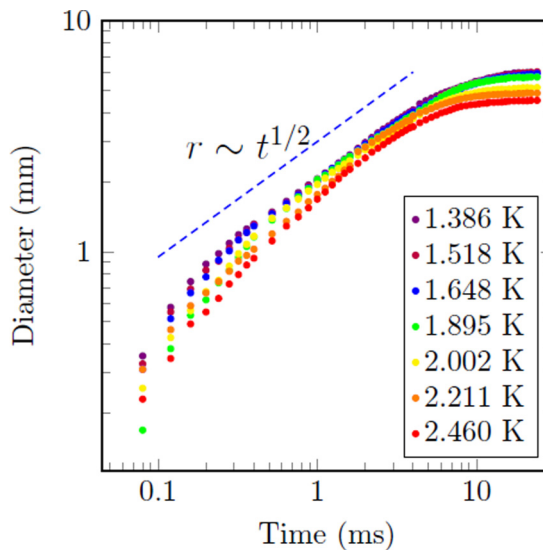


FIG. 3. Drop footprint diameter as a function of time after impact at a velocity of $U = 0.45$ m/s for several values of the ambient temperature indicated by colors ranging from violet (the coldest) to red (the warmest). The dashed blue line shows a growth rate characterized by an exponent of $1/2$, which is typical of many classical fluids. Although the superfluid fraction varies from zero to 0.93, this does not significantly affect the short-term dynamics of spreading. There is a rather abrupt transition to a much slower growth rate near $t \sim 6$ ms.

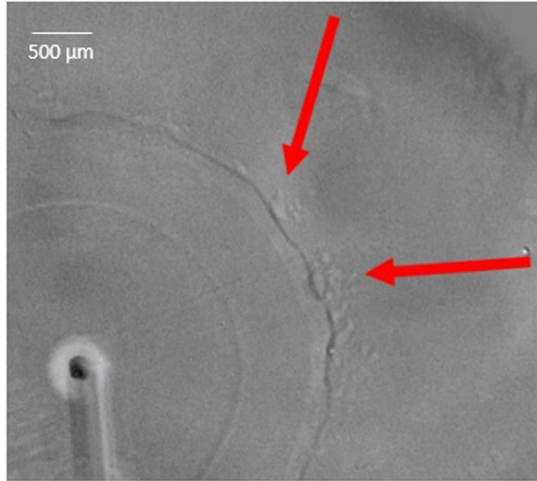


FIG. 4. Bottom view of a spreading superfluid drop at $T = 1.564$ K, with arrows pointing to the ring of exodroplets. Most of the drop is in the lower-left quadrant; the contact line is clearly visible, and the dark spot in the lower left of the photo is the dropper nozzle.

transient satellite droplets around the edges of the spreading drop, shown in a bottom view in Fig. 4. These droplets may be a manifestation of the high-velocity superflow in the thin film surrounding the drop that we discuss in the next section. At the greater impact velocity of $U = 0.94$ m/s, in addition to the appearance of satellite droplets, the drop contact line became ragged and frayed, as shown in Fig. 5.

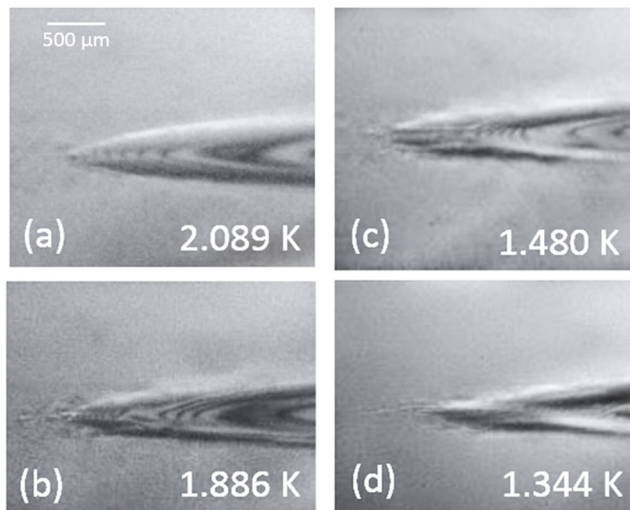


FIG. 5. Side view images of the advancing edge of a drop at four temperatures with the superfluid fraction varying from 0.28 to 0.95. At an impact velocity of $U = 0.94$ m/s, the edges of the drop become progressively more frayed, ragged, and angular at lower temperatures.

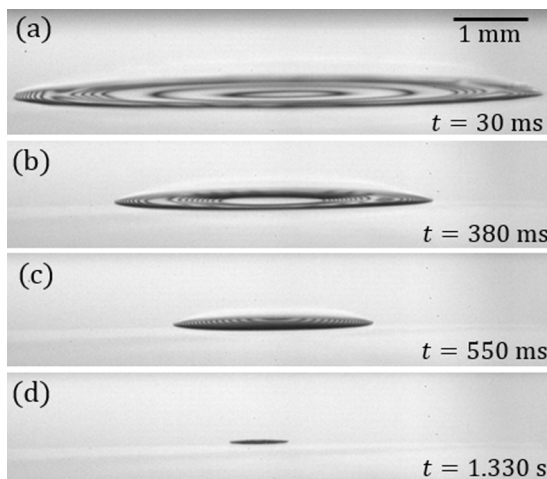


FIG. 6. Side view of a ^4He drop at temperature $T = 1.626$ K contracting on the sapphire substrate at time t after impact. The concentric bands of light and dark are due to interference from regions of different thicknesses; the profile of the drop determined from these interference lines is discussed below. The drop disappears after approximately 1.48 s.

B. Droplet contraction and lifetime

Although superfluidity has only subtle effects on spreading in the first few milliseconds after impact, it has dramatic effects on the subsequent behavior of the drops. After dissipating the initial kinetic energy, conventional liquids on a wettable substrate will continue to slowly spread, with dynamics described by some version of Eq. (1). For volatile drops such as ours, which are surrounded by saturated vapor, the spreading process is eventually truncated by the competing process of evaporation which is driven by the Laplace pressure and the gravitational variation in the vapor pressure in the cell. Above T_λ , helium drops follow this scenario and can be observed to spread for many minutes; the details of this process will be discussed in a subsequent publication. Below T_λ , helium drops begin to contract immediately after the inertia-driven regime and have a lifetime of only a few seconds. Video frames which illustrate the evolution of the drop footprint at $T = 1.626$ K are shown in Fig. 6. The lifetime of the drop is less than 2 s at low temperature, but rapidly diverges near T_λ , as shown in Fig. 7. Figure 8 shows a radius vs time plot for the lifetime of a typical colder drop.

C. Superflow through the surface film

The rapid contraction of the drops cannot be explained by evaporation, which would require pressure differences of the order of 1 Pa or temperature differences of the order of 10^{-4} K, both of which are difficult to justify in our experimental cell. We verified that injecting 5 mW of power into the substrate using the electrical heater had no effect on the drop lifetime. The strong temperature dependence of the drop lifetime near T_λ and the much longer lifetimes in the normal state suggest that the mass transfer mechanism out of the drop is superfluid flow. The basic plausibility of this idea is supported by the rough estimate that flow at a critical velocity of ~ 1 m/s in the surrounding film of thickness 30 nm can drain the 10^{-7} kg mass of the drop in a few seconds. One meter per second is well below the Feynman critical velocity of $v_F \sim 10$ m/s.

A more quantitative understanding of the superflow out of the drop can be obtained by using interferometry to map out the drop topography. The interference lines are like contour lines on a topographical map, connecting regions of equal height above the impact surface. Using the assumptions that the drop thickness is effectively zero at the nominal contact line, the contrast

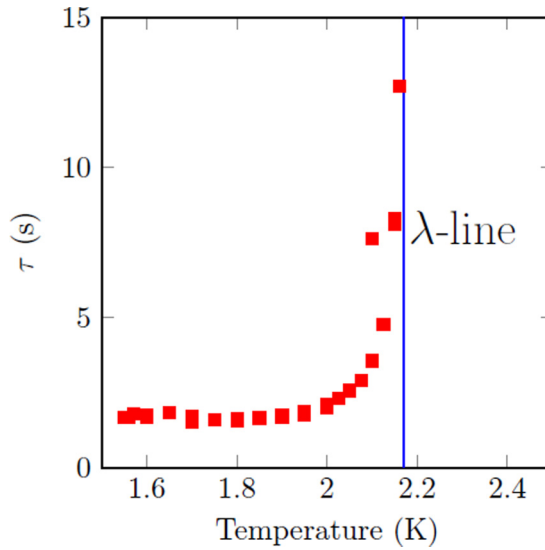


FIG. 7. Superfluid drop lifetime τ on the substrate as a function of temperature. The drops last up to 15 min above the λ line.

in the interference image can be integrated to find the drop thickness at any point in the interior. The ambiguity about the sign of the thickness change corresponding to an intensity change can be reconciled by using the fact that the volume of the drop changes slowly on the timescale of a few milliseconds. In particular, we verify that the volume in the initial falling drop shown in Fig. 2(a) is the same as the volume of the drop after the inertia-driven spreading phase shown in Fig. 2(c).

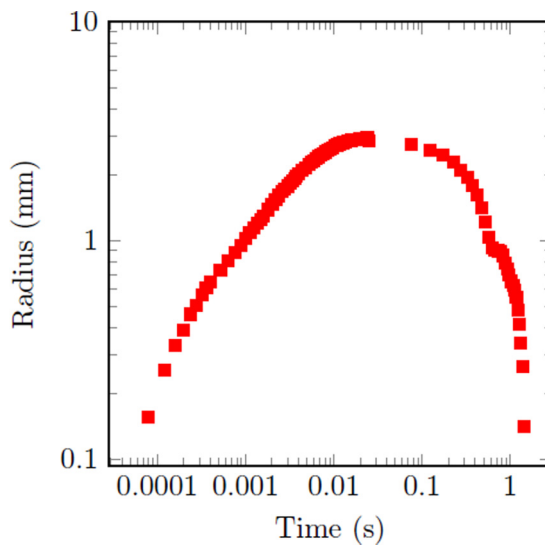


FIG. 8. Total drop lifetime (radius vs time) created by combining two drops filmed at different frame rates, with a drop at $T = 1.648$ K plotted here for the short-term spreading and a drop at $T = 1.626$ K plotted to show the two-phase contraction. The linear phase of the two-phase contraction appears curved here because this is a log-log plot.

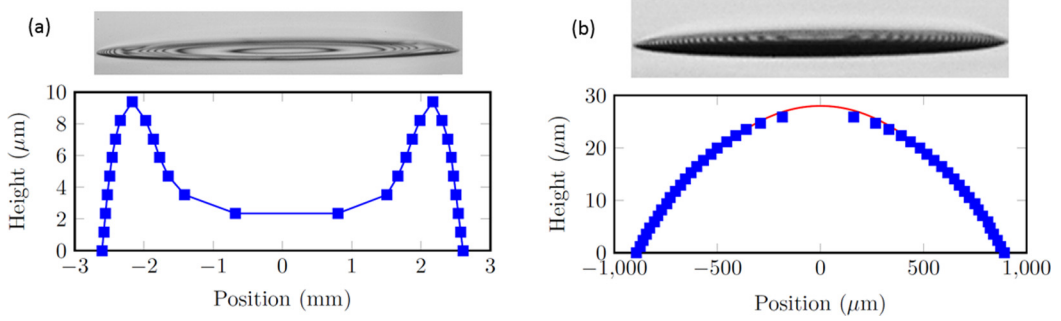


FIG. 9. Images of a drop at $T = 1.626$ K with plots of the cross-sectional profile computed from interference lines, with each data point in the plots corresponding to a dark fringe in the image. Panel (a) shows the drop during the toroidal phase, and panel (b) shows the drop during the spherical cap phase. The red line in panel (b) is a fit to a circle. Note that the horizontal scale in both panels (a) and (b) is orders of magnitude larger than the vertical scale, so the drops are actually very flat. The drop has lost about 60% of its original volume by the time it reaches the spherical cap phase.

Figure 9 shows the drop profile constructed in this way for a drop at the beginning of the contraction process. In the toroidal phase shown in Fig. 9(a), the maximum thickness regions (typical scale $\sim 10 \mu\text{m}$) of the drop are near the contact line, and the center of the drop is thinner. Figure 9(b) shows the profile near the end of the drop lifetime, where the drop has evolved into a spherical cap shape with a peak height approximately twice that of the toroidal rim.

More details of the drop profiles as a function of time and temperature are shown in Fig. 10. These data show that in the toroidal phase the receding contact angle is quite constant in time

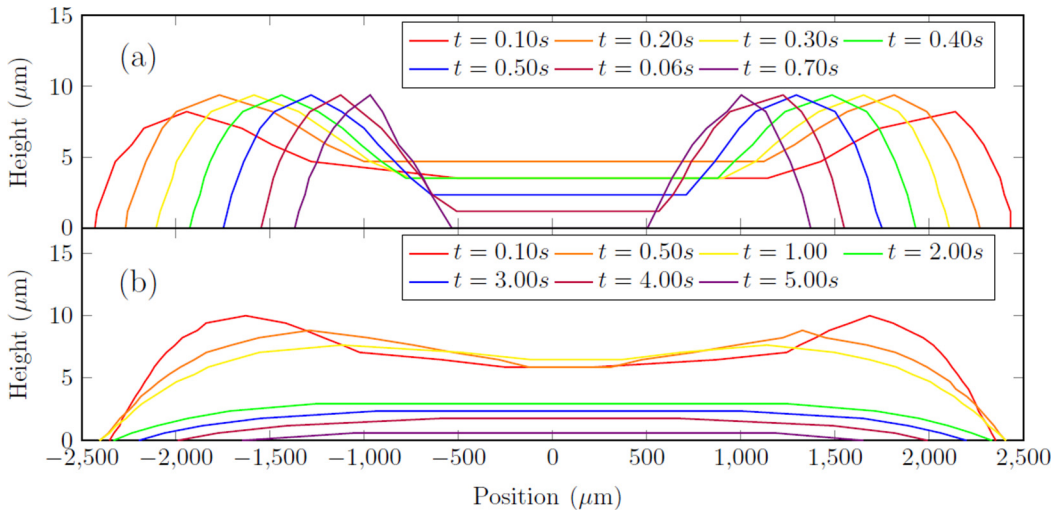


FIG. 10. Evolution in time of drop profiles at time t after impact for temperatures (a) $T = 1.7991$ K and (b) 2.1495 K; note the longer timescale in panel (b). Contraction for colder drops was characterized by a constant contact angle (as can be seen by the parallel drop profiles in time), a radius that contracts linearly with time (shown by the equal linear distance in time between profiles), a constant height, a very short lifetime, and a “donut hole” that forms in the middle of the drop as it drains. By contrast, drops near T_λ (which contain a very small fraction of superfluid) underwent a “deflation” where the drops appear to collapse on themselves as the fluid drains more slowly than with the colder drops.

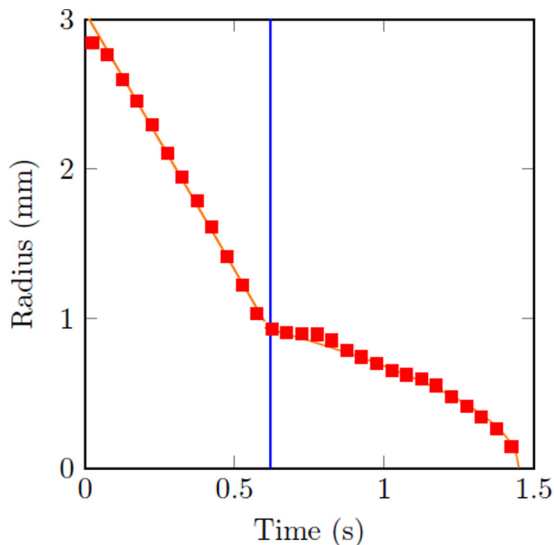


FIG. 11. Radius vs time for a contracting superfluid drop at $T = 1.626$ K. The linear behavior from 0 to 0.6 s corresponds to the contraction of the toroidal drops with constant contact line velocity. The change in behavior at $t = 0.6$ s (marked by the blue vertical line) is the transition to a spherical cap shape. The orange line is a fit for the data.

as the drop footprint shrinks. As the drop shrinks, the radius of the central region decreases and it becomes thinner until an instability occurs and the drop makes a rapid and somewhat violent transition to a spherical cap drop, as shown in Fig. 9(b). This transition between two is also apparent in plots of the drop footprint radius as a function of time, as shown in Fig. 11. The plot shows that the radius initially decreases linearly with time and then makes an abrupt transition to a different regime in which the shrinking rate slows down but then accelerates again near $t = \tau$, the lifetime of the drop. Both of these behaviors are qualitatively consistent with simple geometrical models and the assumption that the superflow is carried by a surface film of constant thickness h moving at a critical velocity, v_{crit} . To explain the linear phase, we make a dimensional argument. The drop shape on the surface is not quite cylindrical, but we make the approximation that the drop footprint is circular and that the profile of the drop near the contact line is relatively constant in time and has a constant average height, H [a good assumption for colder superfluid drops, as shown in Fig. 10(a)]. The drop volume V and the radius r in time is $V(t) \sim r(t)^2 H$, and the change in volume per unit time is $dV/dt \sim r\dot{r}H$, or $dV/dt \sim v_{\text{crit}}r(t)H$, with $\dot{r} = dr/dt$. It follows that $\dot{r} \sim v_{\text{crit}}$, so the radius contracts linearly in time.

During the second half of the contraction, we empirically observe that the drops contract approximately as

$$r(t) = C_T \sqrt{\tau - t}, \quad (5)$$

with drop radius $r(t)$, time t , constant C_T that depends on the temperature (and thus the superfluid fraction), and total droplet lifetime τ . We again begin with our two assumptions that the fluid again flows out of the drop at v_{crit} and that θ_c remains constant. However, in the spherical cap phase, the drop will contract differently from the toroidal phase because of the different geometry. The volume V_{sc} of a spherical cap is given by

$$V_{\text{sc}}(t) = \frac{1}{6} h \pi [h_{\text{sc}}(t)^2 + 3r(t)^2], \quad (6)$$

with spherical cap height h_{sc} , which is the drop height for spherical cap drops. The slope at the edge of the drop (which for small slopes is the contact angle θ_c) is

$$\theta_c = -\frac{r(t)}{\sqrt{R_c(t)^2 - r(t)^2}}, \quad (7)$$

where $R_c(t)$ is the radius of curvature of the drop. If the contact angle remains constant, then $R_c(t)$ must change in time. To find $R_c(t)$, we substitute it into the equation for the contact angle and set the time derivative equal to zero. The result is that $R_c(t)$ must be proportional to $r(t)$ and both $\sim\sqrt{\tau - t}$. Experimentally, we find that $R_c(t)$ decreases with time and is roughly consistent with this prediction, although precise comparison is difficult because of the lack of resolution as the drops become very small.

Understanding the dynamics of the transition from the toroidal phase to the spherical cap phase is a complicated problem that presumably would require a numerical inviscid solver as, e.g., in Ref. [32]. A qualitative understanding of the receding contact angle can, however, be obtained using a simplified one-dimensional model developed by Herminghaus [26] and Poujade *et al.* [25]. The model is based on several assumptions. First, they assume that the superfluid will respond to a gradient in the chemical potential by generating a flow at a critical velocity which is essentially independent of the magnitude of the gradient. The direction of the flow will be toward lower pressure and/or higher temperature. Assuming a strictly isothermal environment, the chemical potential inside the drop will typically be higher than the bulk fluid in the cell by an amount $\Delta\mu$ (with $\Delta\mu$ representing the difference in chemical potential) due to the higher gravitational potential energy and the increased capillary pressure due to curvature, so we expect a flow out of the drop into the microscopically thin adsorbed film which coats the substrate. Only the superfluid moves in the thin film because the normal component is viscously clamped to the substrate. Another basic assumption is that in quasi steady state the pressure in the vapor at the liquid-vapor interface is constant and can be taken to be zero. The pressure inside the drop is mainly determined by three effects: the Laplace curvature, the van der Waals interaction potential of the fluid with the substrate, and the Bernoulli pressure term which is proportional to $-v^2$, i.e., a high flow velocity corresponds to a low pressure. The flow velocity v is not directly observable, but the superfluid flux $j = \frac{\rho_s}{\rho} v(x) h(x)$ is observable, where x is the coordinate along the substrate normal to the thin film-drop contact line, ρ_s/ρ is the fraction of fluid that is superfluid in the two-fluid model, and $h(x)$ is the height of the liquid-vapor interface. In steady state, j is constant, so v is inversely proportional to the liquid thickness, with $v(x) = \frac{j\rho}{h(x)\rho_s}$. A Lagrangian which describes the difference between the kinetic energy of flow and the potential energy of the fluid is $L = (\rho_s/2)h(x)(\rho/\rho_s)^2 j^2/h(x)^2 - [\Delta\mu h(x) + \gamma\sqrt{1 + h'(x)^2} + Cd/3h(x)^3]$. The Euler equation for this Lagrangian is

$$\Delta\mu = \gamma h''(x) + \frac{C d}{h(x)^4} - \frac{\rho^2}{\rho_s} \frac{j^2}{2h(x)^2}, \quad (8)$$

where the constants $C \sim 4.9 \times 10^{-22}$ J and $d \sim 14$ nm characterize the retarded van der Waals interaction, and $h'(x)$ is assumed to be small. The constant j can be determined from the rate of change of the drop volume. Assuming the drops are axially symmetric, integrating the drop profiles as shown in Fig. 10 yields the drop volume V as a function of time, and then $dV/dt = 2\pi r j$ can be used to calculate j . The results are shown as a function of temperature in Fig. 12, and a schematic of the drop on the surface is shown in Fig. 13.

Equation (8) describes the transition from a nanometer-thick film to a drop of bulk liquid, as illustrated in Fig. 13. Introducing a reduced height, h_r , with $h = h_r\sqrt{2Cd\rho_s}(j\rho)^{-1}$ and a reduced transverse distance, x_r , with $x = x_r(2\rho_s)^{5/4}(Cd)^{3/4}\gamma^{1/2}(j\rho)^{-5/2}$, yields the following

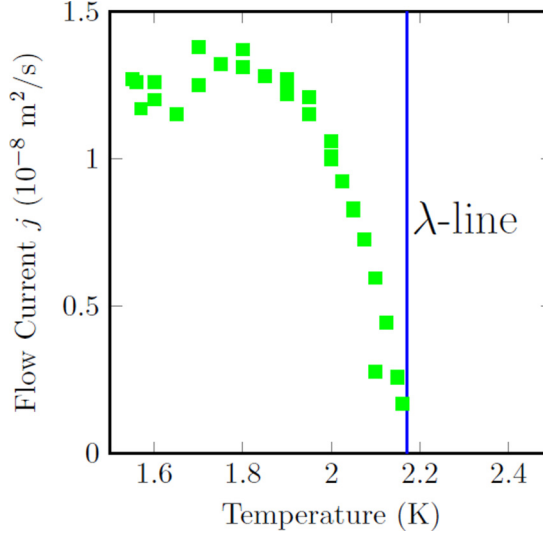


FIG. 12. Flow current j as a function of temperature, calculated from drop lifetime.

nondimensional equation,

$$h_r'' + \frac{1}{h_r^4} - \frac{1}{h_r^2} = A, \quad (9)$$

where $A = 4Cd\delta\mu\rho_s^2/j^4\rho^4$, which for typical drops has a value of ~ 0.01 . This equation has a first integral,

$$\frac{1}{3h_r^3} - \frac{1}{h_r} + Ah_r - \frac{1}{2}(h_r')^2 = \text{const}, \quad (10)$$

where the constant is determined by evaluating the expression in the flat thin film regime where $h_r = 1$ and $h_r' = 0$. If we make the approximation that $A = 0$, $\text{const} = -2/3$, and for large h_r Eq. (10)

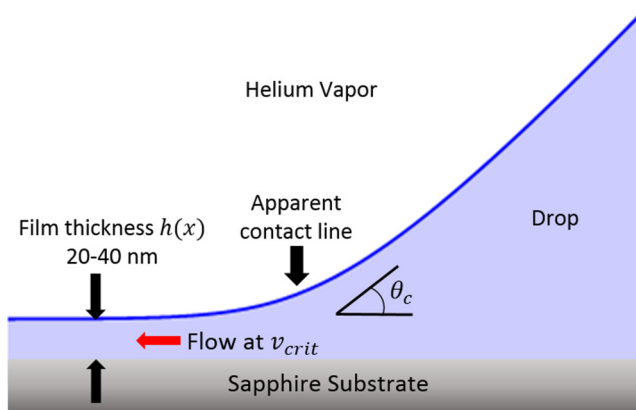


FIG. 13. Cross-sectional schematic of a drop on the substrate showing superfluid flow out of the drop through the thin film at v_{crit} , film thickness $h(x)$, and contact angle θ_c . The pressure at the liquid-vapor interface is zero. The pressure in the thin film region is raised by the van der Waals force, but is lowered overall by the faster-moving flow.

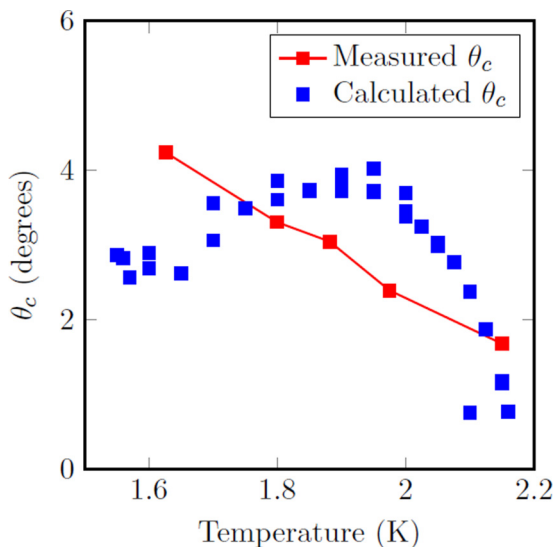


FIG. 14. Comparison of interferometric measurements of θ_c as a function of temperature (in red) with the theoretical prediction of Eq. (11) (in blue). θ_c was measured during the toroidal phase of the drops by fitting the first six dark fringes to a circle and taking the derivative (height vs horizontal distance) at the apparent contact line.

yields $h'_r \sim 2/\sqrt{3} + O(1/h_r)$, this slope defines the contact angle of the bulk liquid drop as it merges into the flat adsorbed film. For small values of the slope, the contact angle θ_c in terms of dimensional parameters [25] is

$$\theta_c = \frac{2^{1/4}(j\rho)^{3/2}}{(3\gamma)^{1/2}(Cd)^{1/4}\rho_s^{3/4}}. \quad (11)$$

If A is nonzero, the shape of the profile is not asymptotically linear as shown illustrated in Fig. 13, but rather grows as $\sqrt{h_r}$, until the profile is eventually flattened by gravity, so a unique asymptotic slope cannot be defined; Eq. (10) is strictly valid only near the contact line. Numerical solutions of Eq. (10) with $0 < A < 0.1$ show that the profile has a linear regime near the contact line which is qualitatively similar to the $A = 0$ case shown in Fig. 13, but with a slope that varies by less than 10%.

The temperature dependence of j is measured in our experiment, and the temperature dependencies of ρ_s and γ are tabulated [33]. A comparison of the predictions of Eq. (11) and the values of θ_c measured from the interferometrically determined profiles is shown in Fig. 14. Our measured values of θ_c agree very well with those of Poujade *et al.* [25], even though their measurements involved a static contact line formed by a plate immersed in the superfluid, while our contact line is dynamic. In both cases, the contact angle within a few millikelvin below T_λ is remarkably high ($\sim 2^\circ$). Poujade *et al.* [25] assumed that j had the same temperature dependence as the superfluid fraction. Our measurements show that the temperature dependence of j is more rapid than the superfluid fraction. For example, at $T = 1.9$ K, j has reached its asymptotic maximum low-temperature value (which roughly agrees with the value assumed by Poujade *et al.* [25]), but the superfluid fraction is less than 0.6. The model which generates the contact angle formula given by Eq. (11) yields the right order of magnitude, but it does not seem to explain the temperature dependence correctly.

IV. CONCLUSION

We have investigated the impact and spreading of superfluid helium drops on a sapphire substrate using video imaging and interferometry. The spreading rate of classical liquids is inversely proportional to the viscosity, so one of our initial goals was to see if the zero-viscosity superfluid spreads differently than the finite-viscosity normal fluid. We observed that the short-term (inertia-driven) spreading of the superfluid is not remarkably fast, but is in fact very similar to the normal fluid because this portion of the spreading is dominated by the balance between the fluid's inertia and surface tension rather than by viscosity. The kinetic energy of the impact is dissipated in about 10 ms even at temperatures where the superfluid fraction is greater than 0.95. Even though helium completely wets all conventional substrates, superfluid drops do not continue to spread with power-law dynamics as most other fluids do. After the inertia-driven phase, superfluid drops do not spread at all, but rather contract and disappear. The lifetime is strongly temperature dependent and ranges from a few seconds at low temperatures to tens of seconds near T_λ . This lifetime is consistent with a model in which the superfluid flows out of the drop through the preexisting nanometer-scale adsorbed film on the substrate. The flow velocity in the film required to explain the drop lifetime is of the order of 1 m/s, which is similar to the critical velocity observed in other nanometer-scale superflows. The contracting superfluid drops have a receding contact angle of several degrees. The existence of a finite contact angle as well as its approximate magnitude is explained by a model which balances surface tension, van der Waals forces, and the Bernoulli pressure in the high-velocity flow in the thin film.

ACKNOWLEDGMENT

This research was supported by King Abdullah University of Science and Technology (KAUST) under Grant No. URF/1/2621-01-01.

-
- [1] C. Josserand and S. T. Thoroddsen, Drop impact on a solid surface, *Annu. Rev. Fluid Mech.* **48**, 365 (2016).
 - [2] R. Rioboo, M. Marengo, and C. Tropea, Time evolution of liquid drop impact onto solid, dry surfaces, *Exp. Fluids* **33**, 112 (2002).
 - [3] P. Kavehpour, B. Ovryn, and G. H. McKinley, Evaporatively-driven Marangoni instabilities of volatile liquid films spreading on thermally conductive substrates, *Colloid Surf., A* **206**, 409 (2002).
 - [4] J. Lopez, C. A. Miller, and E. Ruckenstein, Spreading kinetics of liquid-drops on solids, *J. Colloid Interface Sci.* **56**, 460 (1976).
 - [5] A. L. Yarin and D. A. Weiss, Impact of drops on solid-surfaces: Self-similar capillary waves, and splashing as a new-type of kinematic discontinuity, *J. Fluid Mech.* **283**, 141 (1995).
 - [6] J. E. Sprittles and Y. D. Shikhmurzaev, The dynamics of liquid drops and their interaction with solids of varying wettabilities, *Phys. Fluids* **24**, 082001 (2012).
 - [7] C. Josserand and S. Zaleski, Droplet splashing on a thin liquid film, *Phys. Fluids* **15**, 1650 (2003).
 - [8] A. B. Wang and C. C. Chen, Splashing impact of a single drop onto very thin liquid films, *Phys. Fluids* **12**, 2155 (2000).
 - [9] A. B. Aljedaani, C. Wang, A. Jetly, and S. T. Thoroddsen, Experiments on the breakup of drop-impact crowns by Marangoni holes, *J. Fluid Mech.* **844**, 162 (2018).
 - [10] B. Bennett, A. Shumays, L. Krysa, and J. Maynard, Noise from raindrops: Fundamental studies of bubble entrainment in pure ^4He , *J. Low Temp. Phys.* **113**, 1073 (1998).
 - [11] D. F. Chao and N. L. Zhang, Effects of evaporation and thermocapillary convection on volatile liquid droplets, *J. Thermophys. Heat Transfer* **15**, 416 (2001).
 - [12] S. C. Case and S. R. Nagel, Coalescence in Low-Viscosity Liquids, *Phys. Rev. Lett.* **100**, 084503 (2008).

- [13] K. G. Winkels, J. H. Weijts, A. Eddi, and J. H. Snoeijer, Initial spreading of low-viscosity drops on partially wetting surfaces, *Phys. Rev. E* **85**, 055301(R) (2012).
- [14] P. G. Degennes, Wetting: statics and dynamics, *Rev. Mod. Phys.* **57**, 827 (1985).
- [15] A. M. Cazabat and M. A. C. Stuart, Dynamics of wetting: Effects of surface roughness, *J. Phys. Chem.* **90**, 5845 (1986).
- [16] D. Bonn, J. Eggers, J. Indekeu, J. Meunier, and E. Rolley, Wetting and spreading, *Rev. Mod. Phys.* **81**, 739 (2009).
- [17] R. J. Donnelly, R. N. Hills, and P. H. Roberts, Superflow in Restricted Geometries, *Phys. Rev. Lett.* **42**, 725 (1979).
- [18] J. F. Joanny, Spreading of superfluid drops, *J. Phys.* **46**, 807 (1985).
- [19] E. Cheng, M. W. Cole, J. Dupontroc, W. F. Saam, and J. Treiner, Novel wetting behavior in quantum films, *Rev. Mod. Phys.* **65**, 557 (1993).
- [20] J. E. Rutledge and P. Taborek, Prewetting Phase-Diagram of ^4He on Cesium, *Phys. Rev. Lett.* **69**, 937 (1992).
- [21] D. Ross, J. E. Rutledge, and P. Taborek, Superfluid droplets on a solid surface, *Science* **278**, 664 (1997).
- [22] J. A. Phillips, P. Taborek, and J. E. Rutledge, Experimental survey of wetting and superfluid onset of ^4He on alkali metal surfaces, *J. Low Temp. Phys.* **113**, 829 (1998).
- [23] H. Alles, A. V. Babkin, P. J. Hakonen, J. P. Ruutu, J. T. Salojarvi, and J. P. Saramaki, Spreading of superfluid ^4He on MgF_2 , *J. Low Temp. Phys.* **102**, 21 (1996).
- [24] R. Luusalo, A. Husmann, J. Kopu, and P. Hakonen, Pseudo-contact angles and pinned vorticity in superfluid ^4He , *Phys. B (Amsterdam, Neth.)* **284**, 147 (2000).
- [25] M. Poujade, C. Guthmann, and E. Rolley, Apparent dewetting due to superfluid flow, *Europhys. Lett.* **58**, 837 (2002).
- [26] S. Herminghaus, Can a superfluid droplet spread?, *Europhys. Lett.* **42**, 443 (1998).
- [27] N. B. Speirs, K. R. Langley, P. Taborek, and S. T. Thoroddsen, Jet breakup in superfluid and normal liquid ^4He , *Phys. Rev. Fluids* **5**, 044001 (2020).
- [28] J. Philippi, P. Y. Lagree, and A. Antkowiak, Drop impact on a solid surface: Short-time self-similarity, *J. Fluid Mech.* **795**, 96 (2016).
- [29] G. Riboux and J. M. Gordillo, Experiments of Drops Impacting a Smooth Solid Surface: A Model of the Critical Impact Speed for Drop Splashing, *Phys. Rev. Lett.* **113**, 024507 (2014).
- [30] A. L. Biance, C. Clanet, and D. Quere, First steps in the spreading of a liquid droplet, *Phys. Rev. E* **69**, 016301 (2004).
- [31] A. Eddi, K. G. Winkels, and J. H. Snoeijer, Short time dynamics of viscous drop spreading, *Phys. Fluids* **25**, 013102 (2013).
- [32] M. R. Davidson, Spreading of an inviscid drop impacting on a liquid film, *Chem. Eng. Sci.* **57**, 3639 (2002).
- [33] R. J. Donnelly and C. F. Barenghi, The observed properties of liquid helium at the saturated vapor pressure, *J. Phys. Chem. Ref. Data* **27**, 1217 (1998).